Environmental Pollution 286 (2021) 117534

Contents lists available at ScienceDirect

Environmental Pollution

journal homepage: www.elsevier.com/locate/envpol

Deep learning based regression for optically inactive inland water quality parameter estimation using airborne hyperspectral imagery☆

Chao Niu [a], Kun Tan [a,b,*], Xiuping Jia [c], Xue Wang [a]

[a] Key Laboratory of Geographic Information Science (Ministry of Education), East China Normal University, Shanghai, 200241, China
[b] NASG Key Laboratory of Land Environment and Disaster Monitoring, China University of Mining and Technology, Xuzhou, 221116, China
[c] School of Engineering and Information Technology, the University of New South Wales, Canberra, ACT, 2600, Australia

ARTICLE INFO

Keywords:
Optically inactive water quality parameters
Airborne hyperspectral imagery
Deep learning based regression

ABSTRACT

Airborne hyperspectral remote sensing has the characteristics of high spatial and spectral resolutions, and provides an opportunity for accurate and efficient inland water qauality monitoring. Many studies have focused on evaluating and quantifying the concentrations of the optically active water quality parameters, for parameters such as chlorophyll-*a* (Chl*a*), cyanobacteria, and colored dissolved organic matter (CDOM). For the optically inactive parameters, such as the permanganate index (COD_{Mn}), total nitrogen (TN), total phosphorus (TP), ammoniacal nitrogen (NH3–N), and heavy metals, it is difficult to estimate the concentrations directly, and the traditional indirect estimation models cannot meet the accuracy requirements, especially in heavily polluted inland waters. In this study, 60 water samples were collected at a depth of 50 cm from the Guanhe River in China, at the same time as the airborne data acquisition. We also developed and investigated two deep learning based regression models—a pixel-based deep neural network regression (pixel_DNNR) model and a patch-based deep neural network regression (patch_DNNR) model—to estimate seven optically inactive water quality parameters. Compared with the partial least squares regression (PLSR) and support vector regression (SVR) models, the deep learning based regression models can obtain a superior accuracy, especially the patch_DNNR model, which obtained a superior prediction accuracy for all parameters, with the prediction dataset coefficient of determination (Rp^2) and the residual prediction deviation (RPD) values being greater than 0.6 and 1.6, respectively. In addition, thematic maps of the water quality classification results and water parameter concentrations were generated and the overall water quality and pollution sources were analyzed in the study area. The experimental results demonstrate that the deep learning based regression models show a good performance in the feature extraction and image understanding of high-dimensional data, and they provide us with a new approach for optically inactive inland water quality parameter estimation.

1. Introduction

The ecological environment is one of the most important conditions for the sustainable development of the social economy. Water quality problems caused by point and nonpoint sources of pollutants are particularly prominent, especially in inland water bodies (Brooks et al., 2016; Carpenter and Carpenter, 1983). However, the traditional in-situ sampling approach is labor-intensive and time-consuming, and cannot easily be used to identify the temporal or spatial variations of water quality. Remote sensing has played an important role in the large-scale and long time-series monitoring of inland water, and it provides us with an intuitive and reliable method for regional water quality monitoring and management (Palmer et al., 2015; Ritchie et al., 2003; Tyler et al., 2006).

Differing from ocean and coastal water quality estimation, the area of inland water quality estimation is usually small, so the remote sensing data used for inland water quality estimation need to meet a certain spatial resolution. Multispectral and high-resolution remote sensing sensors are commonly used for inland water quality estimation (Brezonik et al., 2005; Chen et al., 2017; Dekker, 1993; Li et al., 2015). However, limited by the spectral resolution, it is difficult to extract effective spectral features for multiple water quality parameters and

☆ This paper has been recommended for acceptance by Charles Wong.

* Corresponding author. Key Laboratory of Geographic Information Science (Ministry of Education), East China Normal University, Shanghai, 200241, China.
E-mail address: tankuncu@gmail.com (K. Tan).

https://doi.org/10.1016/j.envpol.2021.117534
Received 25 January 2021; Received in revised form 5 May 2021; Accepted 17 May 2021
Available online 6 June 2021

complete multi-parameter water quality estimation with such data. Airborne hyperspectral remote sensing data have the characteristics of high spatial and spectral resolutions, which can help us to identify detailed surface information and extract optical features, and allows us to estimate the concentrations of water quality parameters and trace the source of pollution. As a result, airborne hyperspectral remote sensing data have the potential to be used for water quality monitoring and estimation, especially in rivers, lakes, and reservoirs (Kallio et al., 2001; Koponen et al., 2002; Olmanson et al., 2013; Pyo et al., 2018; Wass et al., 1997).

In the quantitative estimation of water quality, most of the previous studies have focused on optically active variables, such as chlorophyll-*a* (Chl*a*) (Gitelson and Merzlyak, 1997; Xu et al., 2019), cyanobacteria (Kutser, 2004; Pyo et al., 2018; Simis et al., 2005), CDOM (Kutser et al., 2005; Li et al., 2017a), and total suspended matter (TSM) (Dekker et al., 2001; Lei et al., 2020). In view of the active absorption and reflection characteristics, researchers have built estimation algorithms using semi-empirical, semi-analytical, and bio-optical models. The semi-empirical models establish the relationships between the remote sensing data and water quality parameters by selecting characteristic wavebands. The semi-analytical models introduce empirical formulas to retrieve the water quality parameters. The bio-optical models are based on the theory of water radiative transfer, which is used to establish the relationship between the apparent optical properties (AOPs) and the inherent optical properties (IOPs). These models have achieved good results in the estimation and monitoring of the water environment (Gitelson et al., 2008; Gordon et al., 1988; Härmä et al., 2001; Penuelas et al., 1995). However, in addition to these optically active variables, there are also some other important water quality parameters that are optically inactive as they have weak optical characteristics. However, these optically inactive parameters, such as total nitrogen (TN), total phosphorus (TP), ammoniacal nitrogen (NH3–N), the permanganate index (COD_{Mn}), pH, and heavy metals such as cadmium (Cd), nickel (Ni), and zinc (Zn), can be affected by the optically active parameters. These optically inactive water quality parameters are related to water eutrophication, and are of great significance to environmental assessment, especially for human health (Kar et al., 2008; Vakili and Amanollahi, 2020). However, it is difficult to establish the optical characteristics of these parameters directly in the complex bio-optical environment of inland water (Allali et al., 1997; Gholizadeh et al., 2016). Nevertheless, these parameters can be estimated by first establishing the internal correlation with the optically active parameters, and then performing correlation analysis (El Din and Zhang, 2017; El Din et al., 2017). For example, TP and TN can be directly related to Chl*a* concentration and indirectly related to transparency or water clarity (Kutser et al., 1995; Song et al., 2012; Wang et al., 2020). The suspended solids usually act as a carrier for both nitrogen and phosphorus, and they are generally highly correlated (Dekker et al., 2002). The heavy metals in water can exist in a particle form, a dissolved form, and a biological form (Zheng et al., 1982). Furthermore, the distribution of heavy metals in water is controlled by the suspended sediments, phytoplankton, and dissolved organic matter, which implies that the concentration of heavy metals correlates with the spectral properties of water (Chen et al., 2010).

The concentrations of the optically inactive water quality parameters can be estimated using remote sensing. For example, El Din and Zhang (2017) estimated the concentrations of both optically active and optically inactive water quality parameters using Landsat 8 data and a stepwise regression method, and they explored the indirect relationships between the spectral satellite data and the concentrations of the optically inactive water quality parameters. Vakili and Amanollahi (2020) utilized an artificial neural network (ANN) model and a linear regression model to determine the relationship between Landsat 8 Operational Land Imager (OLI) imagery and TP and TN concentrations, and they showed that the ANN model can improve the prediction accuracy for optically inactive water quality variables based on remote sensing data. However, for most of these optically inactive water quality variables, the complex bio-optical environment containing many different water pollutants makes it difficult to find a specific internal correlation between the spectral information and the optically inactive water quality parameters. In this case, the traditional linear and nonlinear regression techniques may not be able to model such complex nonlinear relationships, which is a significant obstacle in the field of inland water quality estimation using remote sensing technology.

With the development of artificial intelligence, machine learning methods have gradually been applied to the field of remote sensing. Due to the unique advantages of machine learning algorithms in solving complex nonlinear problems, many methods such as partial least squares regression (PLSR) and support vector regression (SVR) have been utilized to estimate water quality parameter concentrations (Singh et al., 2011; Song et al., 2013; Sun et al., 2009; Wang et al., 2017; Yang et al., 2020). However, the traditional regression models cannot extract the deep spectral and spatial features of the hyperspectral data, which means that the regression accuracy cannot meet the requirements, and it is impossible to accurately reflect the pollution distribution. Differing from the traditional machine learning methods, deep learning based methods have shown their superiority in remote sensing image classification (Wang et al., 2019) and spectral information reconstruction (Li et al., 2017b). A deep neural network (DNN) model uses multiple hidden layers between the input and output layers to simulate complex nonlinear relationships. As a result, DNN models can be used for the classification and regression of spectral data (Li et al., 2014). The biggest differences between a DNN model and a convolutional neural network (CNN) model are that the CNN model uses convolutional layers to obtain the features of the input data, and the CNN model can capture rich spatial and spectral information when the input data are hyperspectral imagery. Many studies have demonstrated the superiority of CNN models in hyperspectral image classification (Gong et al., 2019; Li et al., 2016). Recently, in a pioneering study, a CNN model was utilized to solve the hyperspectral image regression problem, to estimate the concentrations of phycocyanin and Chl*a* (Pyo et al., 2019). Compared with the bio-optical algorithms, CNN models can obtain a higher prediction accuracy and reasonable spatial distribution results, which shows the superiority of deep learning methods in the feature extraction and image understanding of high-dimensional data.

In this study, we focused on the estimation of multiple water parameters in the complex bio-optical environment of inland water using airborne hyperspectral imagery, and we attempted to find a deep learning model that can accurately estimate multiple water quality parameters through the use of the multi-band characteristics of hyperspectral remote sensing data. Two deep learning based regression models were developed, which have a superior ability to extract the features of high-dimensional data. A patch-based approach is proposed to extract the spatial-spectral information, which makes the deep architecture more effective. Benefiting from the end-to-end learning and nonlinear mapping characteristics, the proposed algorithm has the potential to be used for optically inactive water quality parameter estimation. Accordingly, the aims of this study were: 1) to investigate the use of deep learning based regression methods with hyperspectral remote sensing images to estimate the optically inactive inland water quality parameters; 2) to compare the accuracy of the deep learning regression methods with that of the traditional regression methods (PLSR, SVR); and 3) to generate spatial distribution maps for these multiple water quality parameters, and analyze the overall water quality and pollution sources in the study area.

2. Materials and methods

2.1. Study area

The study area was chosen as the Guanhe River, which is located in the north of Jiangsu province, China, and flows from southwest to northeast. It is the largest river flowing into the Yellow Sea in the north

of Jiangsu province. The Guanhe River is a natural tidal river, with a stream length of about 77.5 km and a basin area of 8000 km^2. The runoff volume of the Guanhe River is 3.5 billion m^3. It is an important agricultural and fishery production area, as well as being one of the main transfer routes for the industries in the south of Jiangsu province.

The sampling and flight area was located in the 36 km from the upper reaches of the Guanhe River (34.22°N, 119.54°E) to the river mouth (34.46°N, 119.78°E), as shown in Fig. 1a. According to the Chinese Environmental Quality Standards for Surface Water (GB3838-2002), the TN, TP, and ammoniacal nitrogen in the Guanhe River all exceed the standards, to varying degrees. The pollution comes from agricultural, domestic, and industrial sources. There are several industrial parks situated around the Guanhe River, which have different degrees of impact on the water quality. It has also been reported that industrial chemical plants have polluted the Guanhe River, seriously affecting the water quality and posing a high environmental risk to the local aquatic organisms (Han et al., 2018). The water quality of the Guanhe River also affects the health of the local population and the sustainable development of the social economy.

2.2. Data acquisition

2.2.1. Hyperspectral image acquisition

A visible and near-infrared (VNIR) imaging spectrometer developed in China was used for the hyperspectral image acquisition. The sensor parameters are shown in Table S1. Before the flight, a monochromator and integrating sphere were used to carry out accurate spectral calibration and radiation calibration. The acquisition dates for the hyperspectral imagery were November 23 and November 24, 2017, and 31 strips were generated in total.

Geometric correction was completed using airborne position and orientation system (POS) data, and the MODTRAN4 radiative transfer model was utilized for the atmospheric correction. The MODTRAN model solves the radiative transfer function to generate the physical

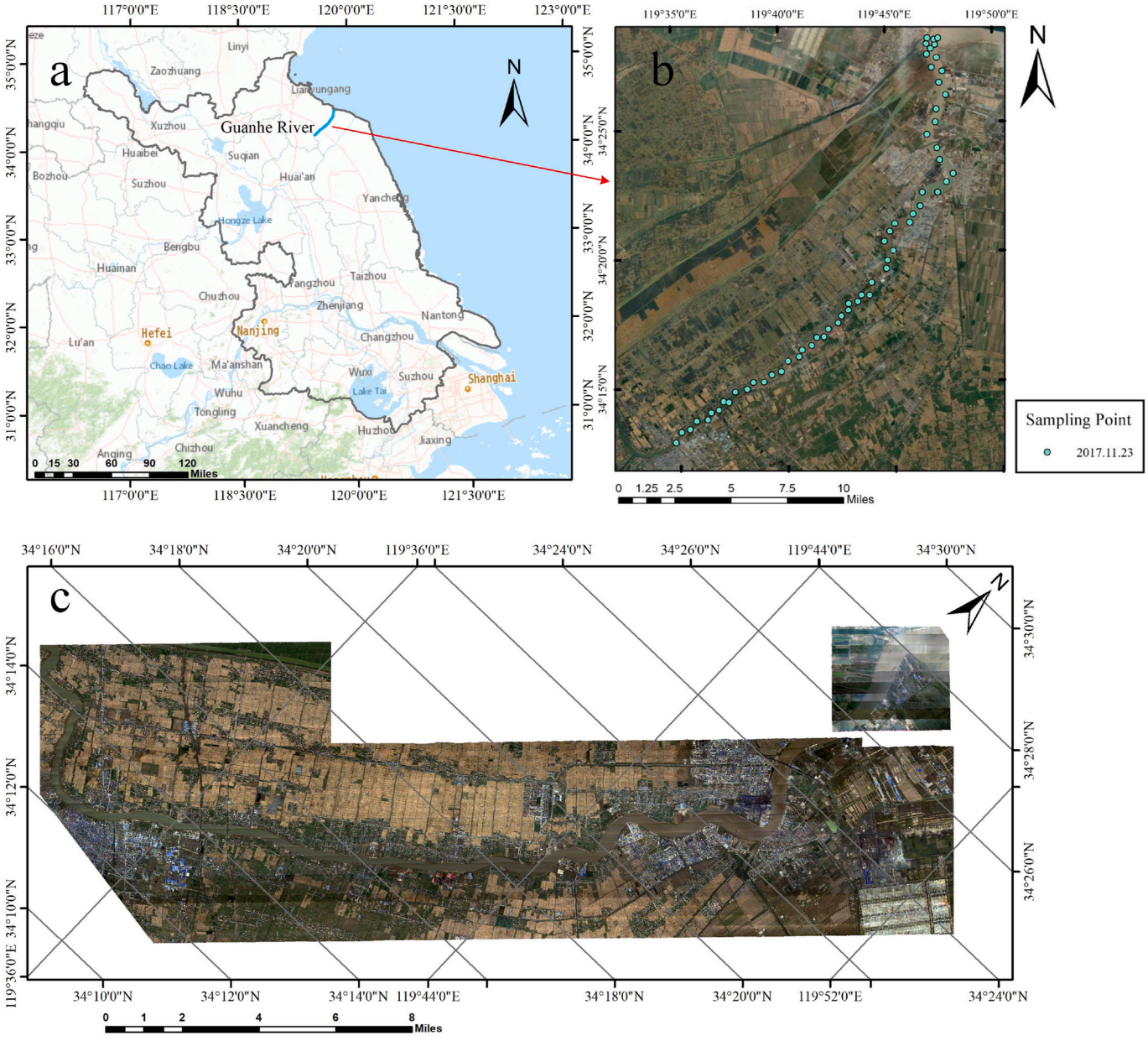

Fig. 1. Geographic location of the study area and the selected sampling positions. (a) Map showing the location of the study area. (b) Map showing the location of the sampling points on the Guanhe River. (c) Mosaicked hyperspectral image after processing.

parameters related to atmospheric correction, such as the transmittance and spherical albedo. Because of the high spectral resolution of the radiative transfer calculation, which can reach a wavenumber of 1 cm^{-1}, it is widely used in the atmospheric correction of hyperspectral images (Keith et al., 2014; Pyo et al., 2018). By acquiring the atmospheric parameters at the time of the flight, including the temperature, humidity, and aerosol optical thickness, and by inputting these parameters into the MODTRAN4 model, the final reflectance image data were obtained with a spatial resolution of 2 m. As the river flows from southwest to northeast, the flight direction was also designed to be southwest to northeast. The final hyperspectral image after mosaicking is shown in Fig. 1c, which has been rotated by 45°.

2.2.2. Field data collection

The locations of the sampling points for the research area were established using a 0.8 × 0.8 km^2 neighborhood grid for each point. In addition, dense sampling points were added in the key areas, such as the industrial areas and the river mouth, as shown in Fig. 1b. At the same time as the flight, 60 water samples were collected synchronously at a depth of 50 cm beneath the water surface and sent to the laboratory for testing. The water quality parameters recorded in the laboratory testing were the three heavy metal elements of Zn, Cd, and Ni, and the four organic parameters of COD_{Mn}, TN, TP, and NH3–N. The test methods were based on the National Standards of China. The specific test methods are listed in Table S2.

2.3. Spectral feature analysis

2.3.1. Spectral pre-processing

The water quality parameter estimation can be regarded as a regression task, with the input being the spectral data after first-order differentiation. After the first-order differentiation, the spectra can better reflect the spectral change information, while the interference of the linear background is suppressed and the overlapping spectral characteristics can be distinguished. Moreover, the first-order differential spectral information can also eliminate the influence of the specular reflection of water bodies, and is an approach that is often used in water quality modeling (Han, 2005; Xing et al., 2013). The formula for first-order differential processing is as follows:

$$R'(\lambda_i) = \frac{R(\lambda_{i+1}) - R(\lambda_{i-1})}{2\lambda_i}, \quad (1)$$

where λ_i is the wavelength; $R'(\lambda_i)$ is the spectrum after first-order differential processing at wavelength λ_i; and $R(\lambda_{i-1})$ and $R(\lambda_{i+1})$ are the spectral reflectance values at wavelength λ_{i-1} and wavelength λ_{i+1}, respectively.

2.3.2. Pearson correlation analysis

The Pearson correlation coefficient is used to express the degree of linear correlation between two variables. The correlation coefficient values range from −1 to 1. Positive and negative numbers indicate positive correlation and negative correlation, respectively. Its absolute value represents the degree of correlation between two variables. The closer the Pearson correlation coefficient is to 1, the stronger the correlation. The Pearson correlation coefficient calculation formula is as follows:

$$r = \frac{\sum_{i=1}^{n}(x_i - \bar{x})(y_i - \bar{y})}{\sqrt{\sum_{i=1}^{n}(x_i - \bar{x})^2}\sqrt{\sum_{i=1}^{n}(y_i - \bar{y})^2}}, \quad (2)$$

where n is the sample size; x_i, y_i are the individual sample points with i; and $\bar{x}, \bar{y}$ are the mean values of the samples.

2.4. Regression methods

In this study, the PLSR linear regression method and three nonlinear regression methods were considered in the comparison. The nonlinear regression methods were SVR and the deep learning based methods of pixel_DNNR and patch_DNNR. In the following, we introduce the parameters and structures of the three nonlinear models.

2.4.1. Support vector regression (SVR)

SVR is the support vector machine (SVM) implementation for regression and function approximation, which has shown its superiority when dealing with multi-dimensional and small sample size datasets (Okujeni et al., 2013; Schölkopf et al., 2002). The main idea behind SVR is to find an optimal approximating hyperplane in the high-dimensional feature space to estimate the linear dependency between the n-dimensional input vectors and the 1-dimensional output variables (Brereton and Lloyd, 2010).

In order to map the data implicitly to a higher-dimensional feature space and make the data fit better, the radial basis function (RBF) was chosen as the kernel function. In the training process for the SVR model, the penalty parameter C and the kernel function parameter g are required to be optimized. Empirically, cross-validation with grid search is the most popular way to search for the best settings for parameters C and g (Chang and Lin, 2011; Zhang et al., 2015). In this study, we determined a wide parameter range (C and g within $[2^{-10},2^{10}]$) with grid search and 5-fold cross-validation, to complete the training of the SVR model.

2.4.2. Pixel-based deep neural network regression (pixel_DNNR)

A DNN is a feed-forward ANN with multiple hidden layers, which are fully connected between the input and output layer (Qian et al., 2014). Many complex regression or classification problems cannot be solved with a single hidden layer, so we have to increase the depth of the network by setting multiple hidden layers. As the multiple hidden layer network architecture has a better ability to represent the data, it can extract deeper features to improve the accuracy of the regression and classification, and can learn patterns from the input data.

In a DNN, there are many connecting neurons in the multiple hidden layers, which can lead to high redundancy, and also difficulty in achieving convergence of the network through the optimization process (Di Noia et al., 2015; Segal-Rozenhaimer et al., 2020). We introduce a residual block to solve the problem of gradient disappearance and gradient explosion caused by the multiple hidden layers. A diagram of the residual block structure is shown in Fig. S1. The input x is connected to the output of the nonlinear layer through shortcut connections, and the final output is $H(x) = F(x) + x$. The stacked nonlinear layers fit another mapping of $F(x) = H(x) - x$, and the original mapping is recast into $F(x) + x$. The residual block can adjust the weight layer and build the identity mapping, which can effectively improve the modeling effect of the deep network (He et al., 2016).

In this study, we designed a pixel_DNNR model with seven hidden layers, and used a rectified linear unit (ReLU) as the activation function. In order to improve the generalization ability of the network, we utilized batch normalization before the activation function of each layer. When training with batch normalization, a training example is seen in conjunction with other examples in the mini-batch, and the training network no longer produces deterministic values for a given training example, which is advantageous to the generalization of the network (Ioffe and Szegedy, 2015). In addition, a dropout layer randomly ignores the output nodes of the prior layer, and the weight and bias are not updated in the backward network, resulting in generalization of the deep learning model and less overfitting of the training dataset (Srivastava et al., 2014).

The network parameters are listed in Table S3. The other parameters, including the learning rate and number of epochs, were adjusted empirically through cross-validation. The deep regression models were

implemented in PyTorch, and the network optimizer was the Adam optimizer with mean-squared error (MSE) loss. The learning rate and epoch number were optimally set to 0.01 and 600, respectively. The architecture of the designed pixel_DNNR model is shown in Fig. 2a. The input is the spectral data of one pixel after first-order differentiation, and the final output value is the parameter concentration.

2.4.3. Patch-based deep neural network regression (patch_DNNR)

Pixel-based DNNs mainly consider the information of single pixels, and the spatial information in the image is ignored (Schwarz et al., 2015). The input of a patch-based deep neural network has three dimensions—height, width, and depth—and by considering the spatial information, patch-based DNNs are more suitable for hyperspectral image processing. The convolutional layer is the core building block of a patch-based DNN, which reduces the amount of parameters and their redundancy through local perception and weight sharing (LeCun and Bengio, 1995).

The multi-dimensional image pixels contain complex and highly heterogeneous spatial and spectral features, and the input patch size affects the feature representation of the patch_DNNR model. Previous studies have found that a relatively small input patch size (8×8) for the regression is more suitable for extracting nonlinear spatial features, without losing heterogeneous information (Pyo et al., 2019). Considering the image resolution and overall image size, the input patch size was set to 9×9 through the optimization.

The network architecture of the patch_DNNR model is described in Table S4. The designed patch_DNNR model is made up of three convolutional layers, one dropout layer, and three fully connected layers. The stride of each convolutional layer is one, while the filter size of the first convolutional layer is 3×3, and that of the other convolutional layers is 2×2. After three layers of convolution and dropout, the extracted deep features are fed into three fully connected layers, and the final output value is the parameter concentration. Batch normalization and the ReLU activation function are utilized in each layer. The parameters of the learning rate, number of epochs, and filter size were adjusted empirically through cross-validation. The learning rate and epoch number were optimally set to 0.01 and 150, respectively. The architecture of the designed patch_DNNR model is shown in Fig. 2b.

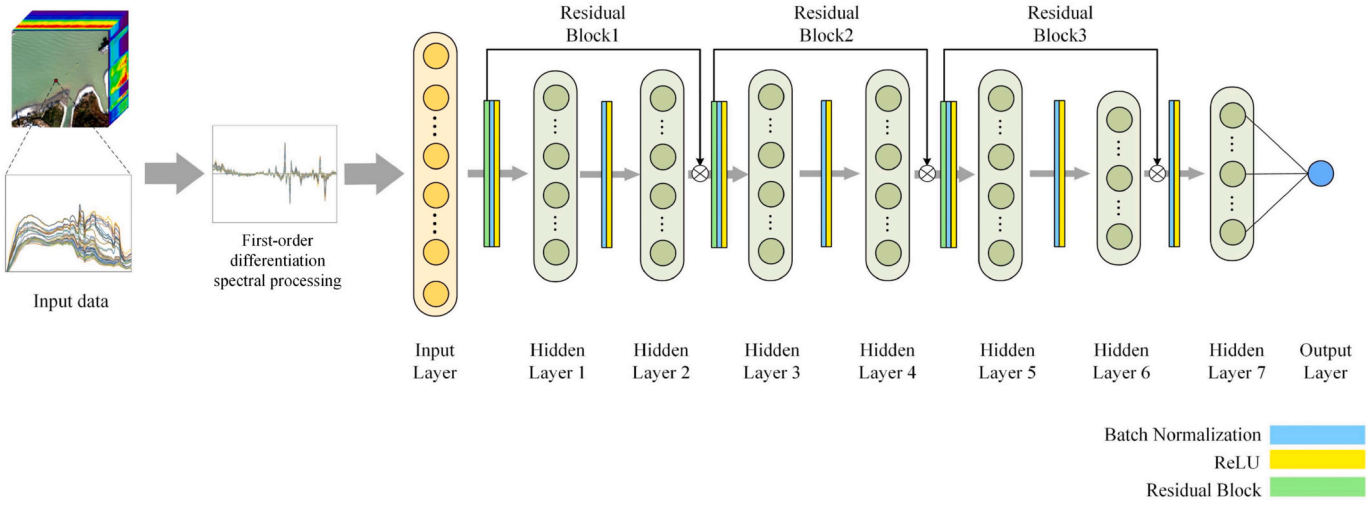

(a)

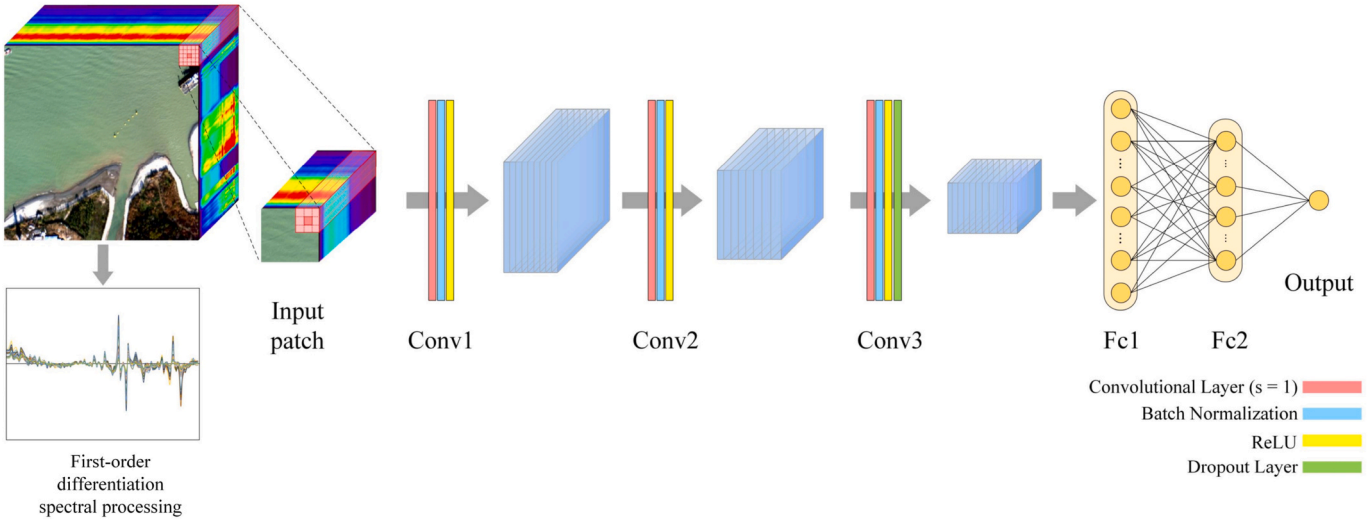

(b)

Fig. 2. The architecture of the designed regression models. (a) The pixel-based deep neural network regression model (pixel_DNNR). (b) The patch-based deep neural network regression model (patch_DNNR).

2.5. Model evaluation

In this paper, the model performance is evaluated by the commonly used regression evaluation indices of the coefficient of determination (R^2), the MSE, the mean absolute error (MAE), the mean normalized bias (MNB), and the residual prediction deviation (RPD). Rc^2, MSEc, MAEc, and MNBc are the evaluation indices for the calibration, while Rp^2, MSEp, MAEp, and MNBp are the evaluation indices for the prediction. The RPD is the ratio of the standard deviation of the prediction dataset (SD_{val}) to the standard error of prediction (Williams, 1987). The indices are calculated as follows:

$$R^2 = 1 - \frac{\sum_{i=1}^{n}\left(\widehat{y}_i - y_i\right)^2}{\sum_{i=1}^{n}\left(\overline{y}_i - y_i\right)^2} \tag{3}$$

$$MSE = \frac{1}{n}\sum_{i=1}^{n}\left(\widehat{y}_i - y_i\right)^2 \tag{4}$$

$$MAE = \frac{1}{n}\sum_{i=1}^{n}\left|\widehat{y}_i - y_i\right| \tag{5}$$

$$MNB = \frac{1}{n}\sum_{i=1}^{n}\frac{\left(\widehat{y}_i - y_i\right)}{y_i} \times 100\% \tag{6}$$

$$RPD = \frac{SD_{val}}{RMSE\sqrt{n/(n-1)}}, \tag{7}$$

where y_i is the measured value, $\widehat{y}_i$ is the predicated value, and n is the number of sample points. In general, a model can be said to perform well if it has higher R^2 and RPD values and lower MSE, MAE, and MNB values.

3. Results and discussion

3.1. Data analysis

The collected water samples were tested by a professional institution, with the basic statistical analysis including the mean value (MEAN), maximum value (MAX), minimum value (MIN), standard deviation (STD), and coefficient of variation (CV). The test results are listed in Table S5. It can be seen that the CV of these parameters is less than 0.6%, which indicates slight data dispersion and the fact that these data are suitable for regression analysis.

To determine if the sample size was large enough, a statistical formula, as shown in Eq. (8), based on the desired power of the analysis was utilized (El Din and Zhang, 2017):

$$n = [(z \times \sigma_x)/\mathrm{ME}]^2, \tag{8}$$

where n is the minimum sample size, z is the value of the standard normal distribution for the desired confidence level (e.g., $z = 1.96$ for a 95% confidence level), and ME is the desired margin of error. At a confidence level of 95%, a desired marginal error of ±2 units, and a maximum standard deviation of 4.41 for the seven measured water quality parameters, $z = 1.96$. Accordingly, the calculated sample size is 18.6, which indicates that the 60 water samples were adequate in this study.

On the basis of the Chinese Environmental Quality Standards for Surface Water (GB3838-2002), inland water quality is divided into five standards—Class I to Class V—of which Class I is the best and Class V is the worst. If the water parameter concentration exceeds the Class 5 standard, it is deemed as "inferior Class 5". Table S6 lists the standard values of the basic items for the environmental quality standards for surface water (the value for Ni is not given in the standards). According to the test results for the sampling points, the statistics for the water quality grades are listed in Table S7. It can be seen from the statistical results that the heavy metal items are all at Class I levels. In terms of the organic parameters, the water quality classification results for TP are between Class III and Class V, of which the Class IV standard accounts for 66.6% and the Class V standard about 26.6%. The classification results for COD_{Mn} are all Class III and Class IV, accounting for 40% and 60%, respectively. Some of the NH3–N and TN samples exceed the Class V standard, and even reach the inferior Class 5 standard, accounting for 36.6% and 85%, respectively. In general, the organic pollution and eutrophication of the Guanhe River can be deemed serious, and the overall water quality for the Guanhe River is inferior Class V.

3.2. Spectral characteristics analysis and curve fitting models

The Pearson correlation coefficients of the spectra after the first-order differentiation were analyzed using single bands and the band ratio. The results of the correlation analysis for the seven water quality parameters are shown in Fig. 3. It can be seen that the concentration values of some of the organic, parameters, such as COD_{Mn} and TN, are closely related to the processed spectra. The high-correlation wavelengths are around 600 nm, 670 nm, 700 nm, 770 nm, and 820 nm. In addition, the absolute value of the correlation coefficients is more than 0.6 around 600 nm–800 nm, which shows the consistent absorption and reflection characteristics for Chl*a* (Gitelson et al., 2008).

The characteristic band with the highest correlation was selected for the curve fitting modeling, to estimate the water quality parameter concentrations. It can be seen from the curve fitting modeling results listed in Table 1 that the R^2 and RPD values are less than 0.6 and 1.2, respectively. Therefore, it is difficult to meet the accuracy requirement for the optically inactive water quality parameter concentration estimation using the spectral feature selection method.

3.3. Comparative analysis of the water parameter estimation models

The dataset used in the experiment was made up of 60 items of spectral data (pixel-based for PLSR, SVR, and the DNNR model, and patch-based for the DNNR model) and laboratory test data, which were randomly divided into a training set (40) and a test set (20) according to the ratio of 2:1. The heavy metals of Zn, Cd, and Ni and the organic pollution parameters of COD_{Mn}, NH3–N, TN, and TP were estimated using PLSR, SVR, the pixel_DNNR model, and the patch_DNNR model. The regression results for these seven parameters are listed in Table 2. The PLSR model shows the worst accuracy, with the Rp^2 values all less than 0.6, expect for TN. The SVR model shows good regression results for Zn, COD_{Mn}, and TN, but it cannot meet the accuracy requirements for the other parameters. The pixel_DNNR model performs better than SVR, and obtains good regression results, except for Ni and NH3–N. Differing from the SVR model and pixel_DNNR model, the input of the patch_DNNR model is patch-based spectra. The patch_DNNR model obtains a high prediction accuracy for all seven water quality parameters, with the Rp^2 values and the RPD values being greater than 0.6 and 1.6, respectively, and it shows the best regression performance. The scatter plots for the observed water quality parameter values and the predicted values of the patch_DNNR model are shown in Fig. 4.

Overall, comparing the accuracy of the three models, it can be seen that the deep neural network regression models (pixel_DNNR, patch_DNNR) can identify the deep spectral features of the optically inactive water quality parameters, and the regression accuracy is greatly improved when compared with the results of the traditional machine learning based PLSR and SVR models. Moreover, the patch_DNNR model performs better than the pixel_DNNR model, which indicates the robustness and accuracy of the designed patch_DNNR model in solving complex regression problems.

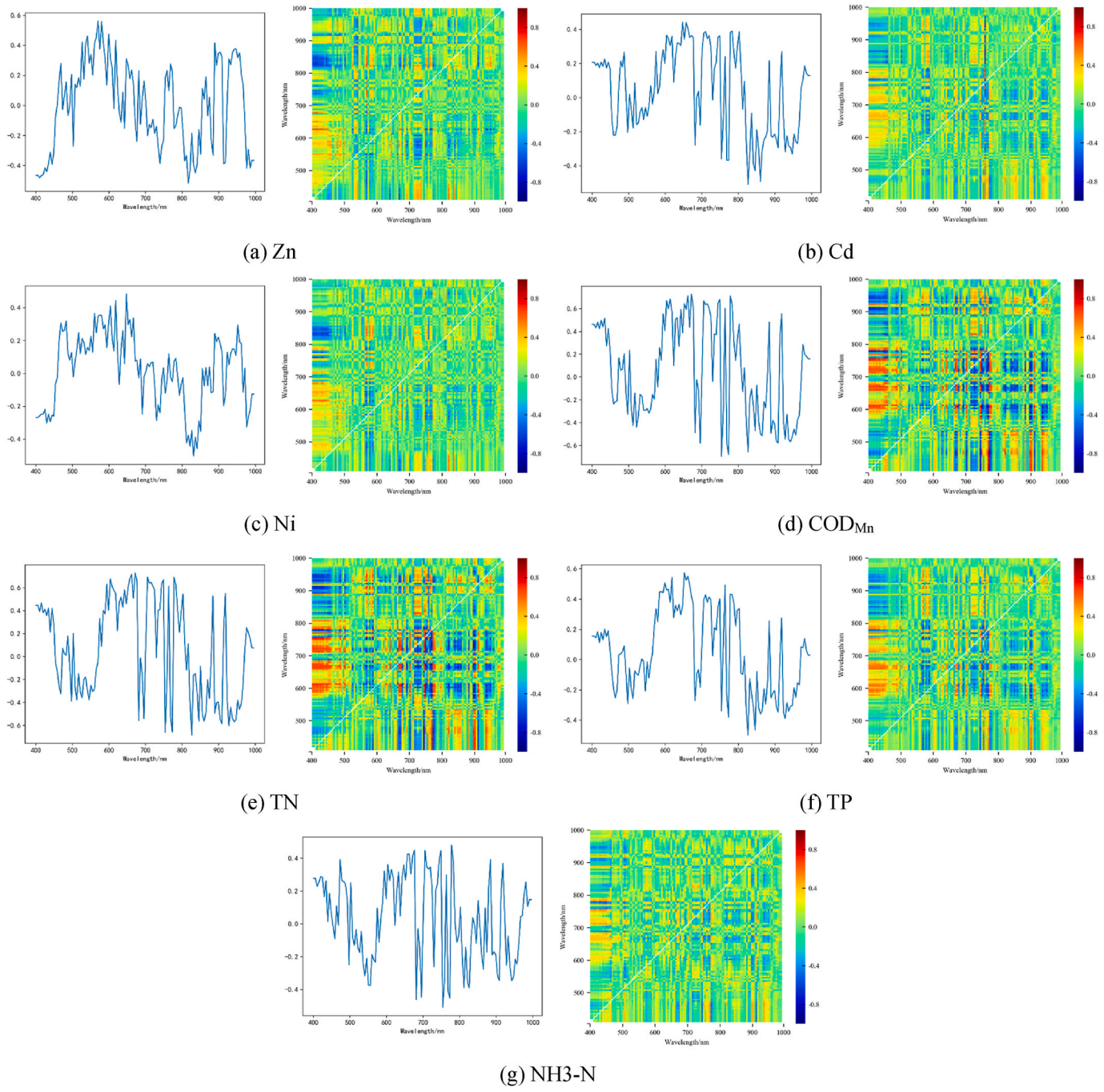

Fig. 3. The correlation of single bands and the band ratio after the first-order differential pre-processing. (a) Zn, (b) Cd, (c) Ni, (d) COD_{Mn}, (e) TN, (f) TP, and (g) NH3–N.

Table 1
Curve fitting results for the water quality parameters.

Parameter	Modeling formula	Selected wavelength	R^2	MSE	MAE	MNB	RPD
Zn	$y = -0.0808x^2 + 2.1047x + 2.7453$	x = 826.54/570.09	0.4128	11.2566	2.6451	16.4807	0.8382
Cd	$y = -1.9955x + 0.1932$	x = 826.54	0.2585	0.0001	0.0087	0.3086	0.5905
Ni	$y = 4.0208e^{-0.453x}$	x = 831.38/429.76	0.3417	1.0583	0.7824	1.73	0.6941
COD_{Mn}	$y = 421.21x + 3.4429$	x = 671.70	0.5287	0.5557	0.6368	1.5425	1.0592
TN	$y = -61964x^2 + 1359.6x - 2.6174$	x = 671.70	0.5705	0.6057	0.6314	5.4216	1.1525
TP	$y = -0.002x^2 + 0.0403x + 0.1309$	x = 753.96/570.09	0.4178	0.0014	0.0298	2.3324	0.8611
NH3–N	$y = 0.8996x + 0.645$	x = 778.15/429.76	0.2759	0.3928	0.4806	14.9260	0.6172

Table 2
Regression results for the water quality parameters.

Water quality parameter	Method	Rc^2	MSEc	MAEc	MNBc	Rp^2	MSEp	MAEp	MNBp	RPD
Zn	PLSR	0.7634	4.8544	1.7006	−3.4963	0.4404	9.1986	2.6598	−8.7651	1.4124
	SVR	0.9266	1.5377	0.4217	1.0254	0.7034	4.5838	1.7638	5.8942	1.8042
	pixel_DNNR	0.9701	0.6198	0.6595	0.7827	0.7207	4.4651	1.7396	7.4872	1.8367
	patch_DNNR	**0.9509**	**1.0123**	**0.4937**	**0.8220**	**0.8828**	**1.8960**	**0.7981**	**−5.4661**	**2.7279**
Cd	PLSR	0.2167	0.0002	0.0097	2.1062	0.1980	0.0001	0.0078	5.0944	1.2177
	SVR	–	–	–	–	–	–	–	–	–
	pixel_DNNR	0.7529	0.0001	0.0004	0.1328	0.6255	0.0002	0.0101	1.8237	1.6388
	patch_DNNR	**0.6961**	**0.0001**	**0.0063**	**−0.5263**	**0.7209**	**0.0001**	**0.0051**	**−0.5367**	**1.8931**
Ni	PLSR	0.8116	0.3338	0.4424	0.0513	0.2528	0.9474	0.6973	4.0442	1.2386
	SVR	0.9374	0.1282	0.1711	−0.0173	0.3382	1.1579	0.5791	−5.7684	1.2866
	pixel_DNNR	0.7241	0.4112	0.5360	0.1047	0.4598	0.8908	0.7965	3.3765	1.4328
	patch_DNNR	**0.8041**	**0.3166**	**0.4434**	**−0.0405**	**0.7956**	**0.3245**	**0.4398**	**−1.9035**	**2.2121**
COD_{Mn}	PLSR	0.8736	0.1667	0.3362	1.4032	0.4897	0.4568	0.5941	6.7809	1.4203
	SVR	0.7296	0.3341	0.4089	2.3466	0.5678	0.4446	0.5610	−3.0733	1.4822
	pixel_DNNR	0.8498	0.1619	0.3335	−1.8763	0.7227	0.3317	0.4671	4.0494	1.8463
	patch_DNNR	**0.9373**	**0.0724**	**0.1785**	**0.2131**	**0.8439**	**0.1902**	**0.2700**	**3.2312**	**2.5311**
TN	PLSR	0.8881	0.1666	0.3388	−4.1478	0.6129	0.4676	0.5718	9.0966	1.6754
	SVR	0.9124	0.1314	0.2087	2.4598	0.6950	0.3207	0.4777	−7.0413	2.1774
	pixel_DNNR	0.9311	0.0986	0.2241	3.0378	0.8281	0.2349	0.3762	6.0679	2.7867
	patch_DNNR	**0.9821**	**0.0248**	**0.1163**	**2.2942**	**0.9394**	**0.0806**	**0.1814**	**4.2852**	**4.0636**
TP	PLSR	0.6732	0.0003	0.0218	2.0117	0.4507	0.0012	0.0312	4.0674	1.4742
	SVR	–	–	–	–	–	–	–	–	–
	pixel_DNNR	0.9578	0.0001	0.0008	0.2308	0.7724	0.0004	0.0164	2.3669	2.0472
	patch_DNNR	**0.8914**	**0.0002**	**0.0129**	**−1.4593**	**0.8677**	**0.0003**	**0.0145**	**−2.2867**	**2.7497**
NH3–N	PLSR	0.7823	0.1059	0.2663	4.7965	0.3899	0.3761	0.4617	8.0437	1.3421
	SVR	0.9864	0.0091	0.0936	3.7687	0.0926	1.2557	1.3845	12.3478	1.1624
	pixel_DNNR	0.9974	0.0010	0.0241	3.4388	0.4895	0.4368	0.5245	−8.7246	1.4682
	patch_DNNR	**0.6401**	**0.1903**	**0.3543**	**5.7231**	**0.6189**	**0.2167**	**0.3469**	**7.8709**	**1.6199**

(The "-" in the table indicates that the Rp^2 is less than 0.01).

3.4. Water quality parameter estimation for the airborne hyperspectral imagery

After comparing the accuracies of the different regression models, the trained patch_DNNR model was applied to estimate the water quality parameters for the airborne hyperspectral images of the study area. The spatial distribution of the seven water quality parameters is shown in Fig. 5. It can be seen that the estimated high-value areas are distributed in the lower reaches of the Guanhe River and around the river mouth, and the estimated pollution in the upper reaches of the Guanhe River is relatively light. Except for Ni, the other parameters were classified into the six pollution classes of the Chinese Environmental Quality Standards for Surface Water (GB3838-2002), as shown in Table S6. The water quality classification maps for the Guanhe River are shown in Fig. 6. The water quality classification results for Zn and Cd are shown in Fig. 6a and b, where the overall water quality is Class I. For the organic water quality parameter of COD_{Mn}, as shown in Fig. 6c, the water quality is Class III to IV. For the TN in the study area, the pollution is serious, and this parameter is generally the inferior Class V, as shown in Fig. 6d. It can be seen from Fig. 6e that the Class V water is distributed in the middle and lower reaches and near the river mouth. The NH3–N pollution is also serious, and the water quality in the middle and lower reaches also reaches inferior Class V.

3.5. Analysis of the pollution sources

Through on-site investigation, we established that there are two large industrial parks and residential areas in the heavily polluted area, as shown in Fig. 7. There are more than 100 enterprises in the industrial parks, including printing and dyeing, pharmaceutical and cosmetic, pesticide, and other industries. Industrial parks can have different degrees of environmental problems, such as wastewater discharged without treatment, illegal disposal of hazardous waste, etc. The Guanhe River is also surrounded by large areas of farmland, in addition to poultry and livestock plants. Synthetic chemical fertilizer is the main source of nitrogen in water, and a large volume of unused nitrogen compounds from crops can enter groundwater and surface water by farmland drainage and surface runoff. When the urine and feces of poultry, livestock, and aquatic animals are discharged into a water body without treatment, the TN and NH3–N in the water body can easily exceed the standards.

In our study area, the pollution situation for TN, TP, and NH3–N is serious. The overall spatial distributions of these parameters are roughly the same, i.e., light in the upper reaches and serious in the middle and lower reaches. The TN pollution is the most serious, and the inferior Class V makes up more than 90% of the total. In addition, the maximum concentration is more than twice the value of the Class V standard. The NH3–N pollution is also serious in the middle and lower reaches, where the inferior Class V standard accounts for more than 40%, and the maximum concentration is more than twice the value of the Class V standard. Compared with TN and NH3–N, the TP pollution is lighter, but the water quality in the middle and lower reaches of the region also reaches Class V. The main problems for the water environment of the Guanhe River Basin are as follows:

1. Industrial pollution sources are widely distributed in the research area, and a large amount of industrial wastewater is discharged indiscriminately into the river, without any treatment, resulting in serious pollution in the lower reaches of the Guanhe River.
2. Agricultural pollution, including pollution from crop production, aquaculture, and livestock breeding, is also serious. The amount of agricultural pollution sources discharged into the river is huge, resulting in the levels of TN, TP, and NH3–N exceeding the standards by a significant margin.
3. The Guanhe River Basin is densely populated, and the industrial parks attract a large number of migrant workers, which leads to an increase in domestic sewage discharge.

3.6. Limitations and future prospects

In this study, our main concerns were establishing the pollution status of the research area quickly and accurately, estimating the

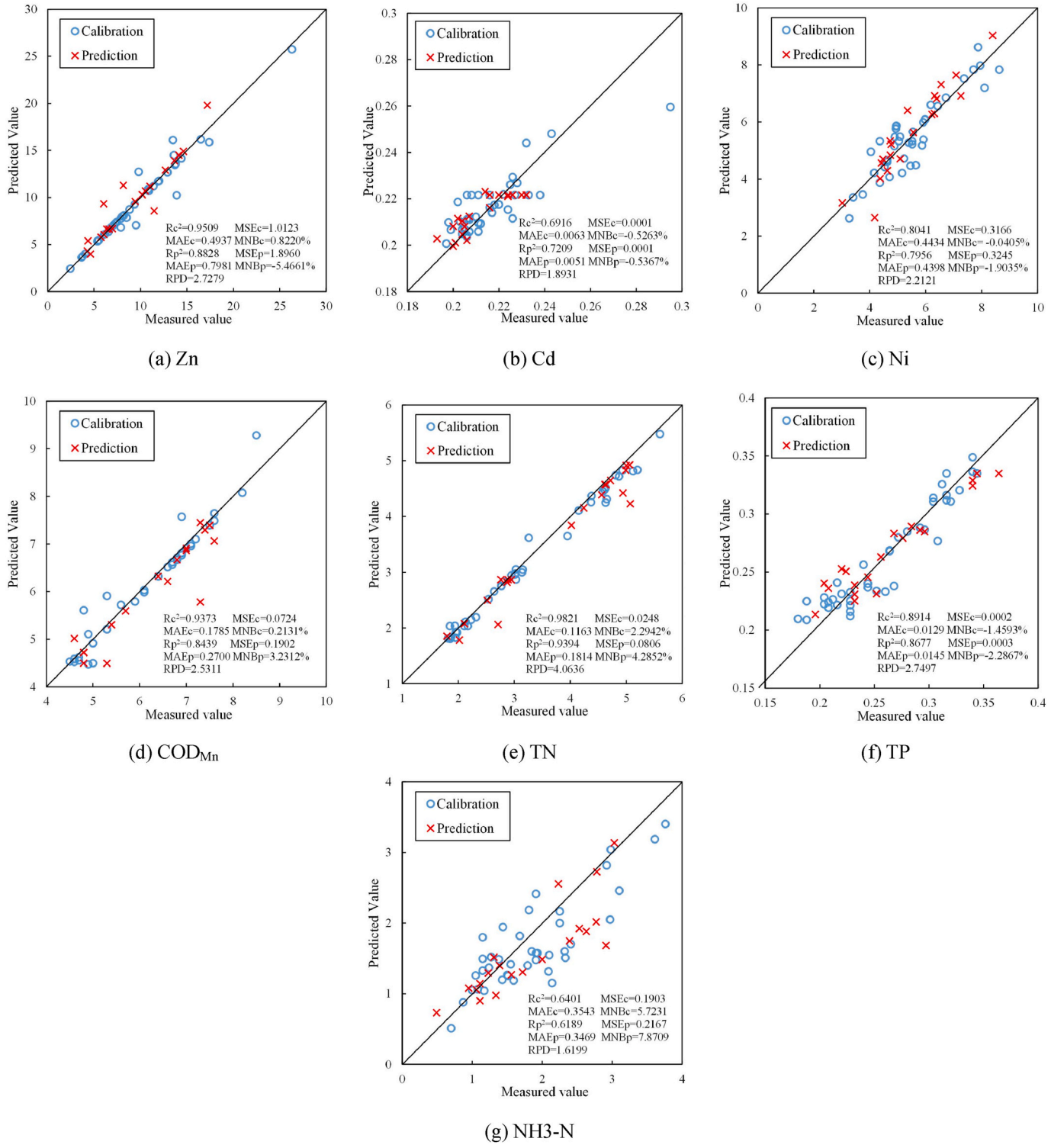

Fig. 4. Scatter plots of the observed water quality parameter values and the estimated values predicted by the patch_DNNR model for: (a) Zn, (b) Cd, (c) Ni, (d) COD_{Mn}, (e) TN, (f) TP, and (g) NH3–N.

optically inactive water quality parameter concentrations, and mapping the distribution of the pollution. Because only one temporal period of hyperspectral image data of the study area was obtained in this study, this scenario was more suitable for quickly establishing the water quality of the river and tracing the pollution sources, rather than building a universal water quality estimation model. However, for a study area with a high concentration of suspended solids, and for locations where the atmospheric absorptive aerosol effect affects the accuracy of the atmospheric correction, the water surface reflectance obtained by the traditional atmospheric correction method would be affected, resulting in a reduction in the model accuracy. In addition, some common rules for optically inactive inland water parameter estimation based on deep learning regression and airborne hyperspectral images need to be further explored. In the future, we will attempt to establish an atmospheric correction method for use in a turbid water scenario, and we will explore the effect on the model precision of water bodies with different

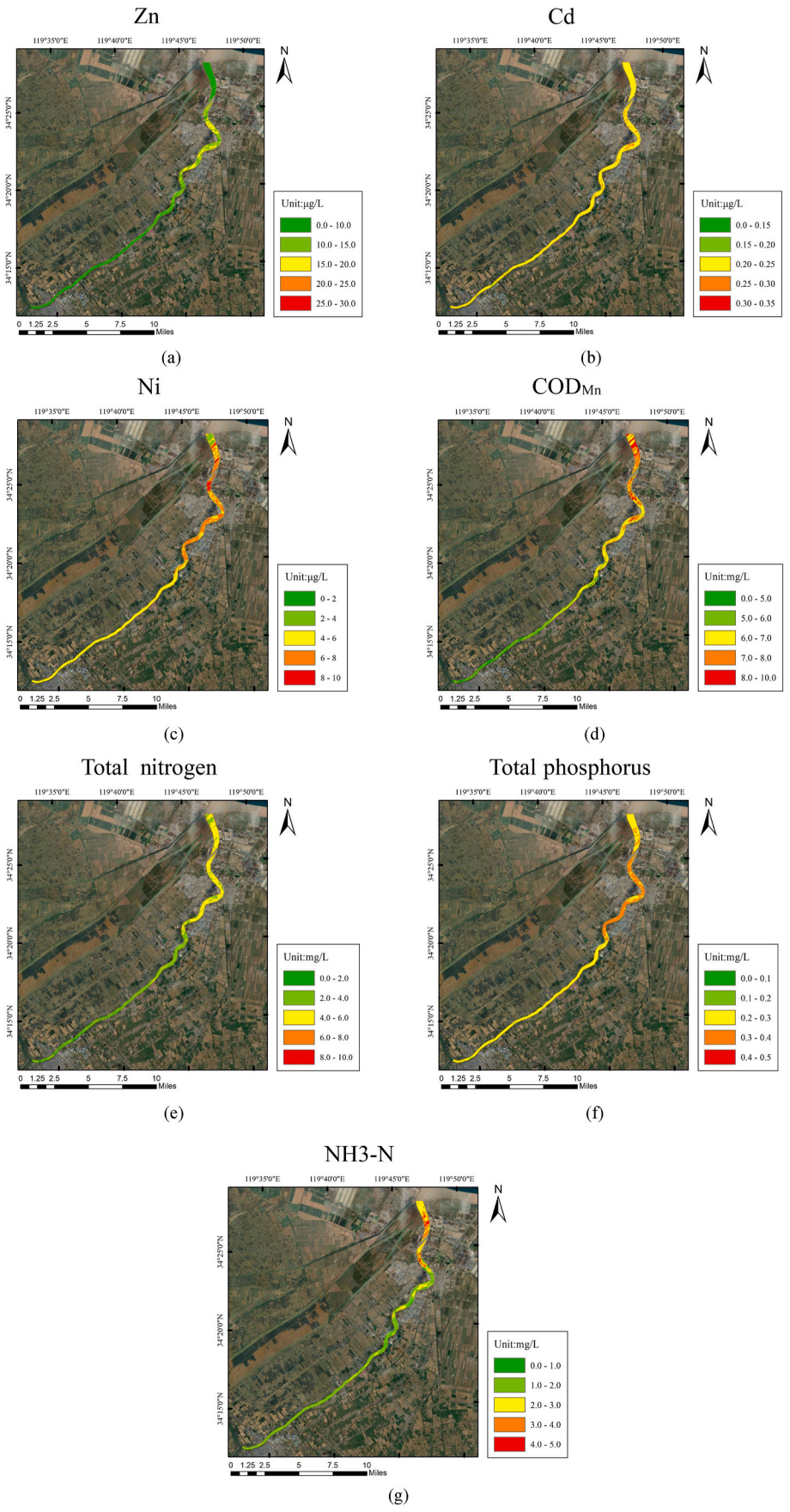

Fig. 5. Water quality parameter concentration spatial distribution maps for the Guanhe River: (a) Zn, (b) Cd, (c) Ni, (d) COD_{Mn}, (e) TN, (f) TP, and (g) NH3–N.

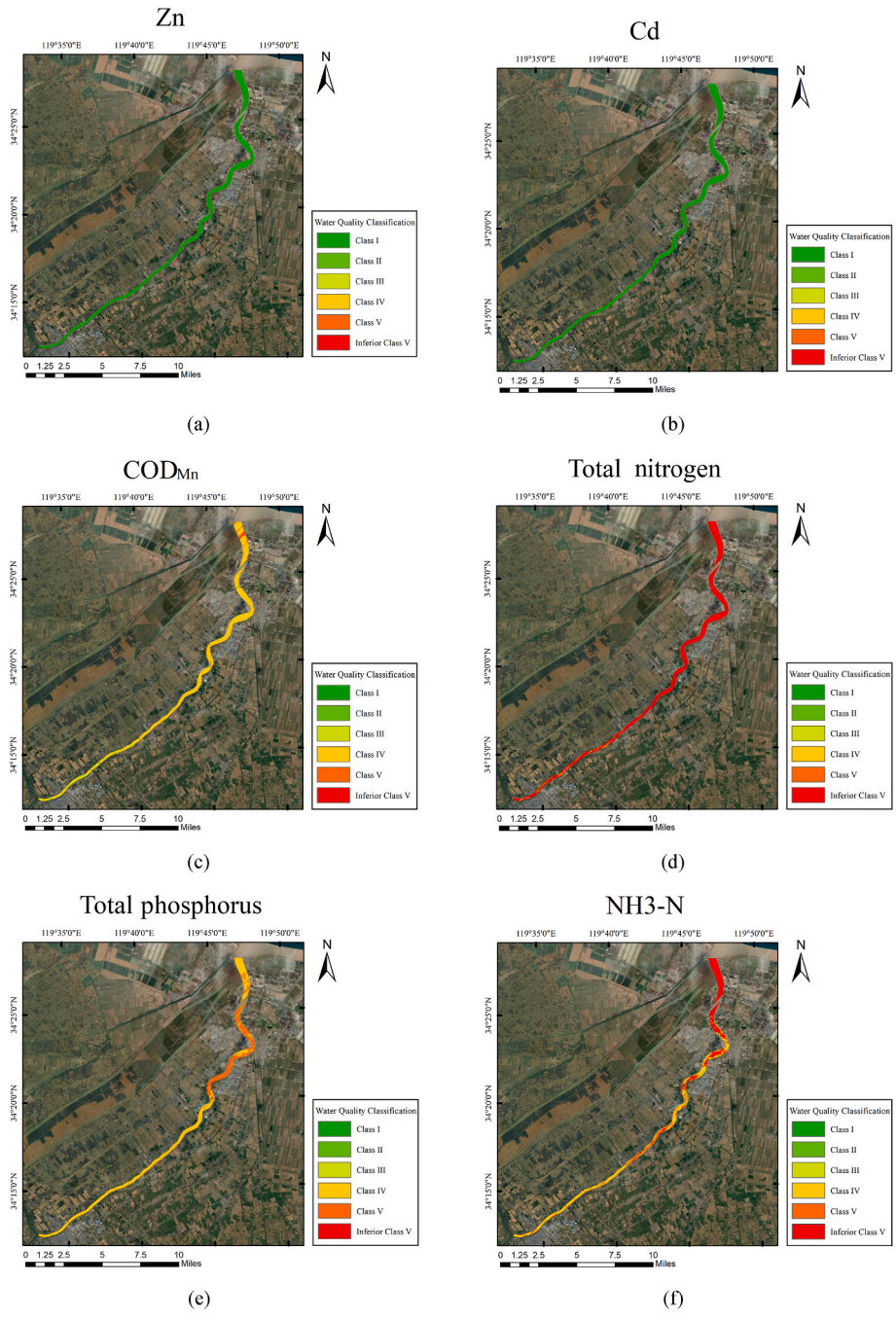

Fig. 6. Water quality parameter classification maps for the Guanhe River. (a) Zn, (b) Cd, (c) Ni, (d) COD_{Mn}, (e) TN, (f) TP, and (g) NH3–N.

turbidity levels. We will also introduce some optically active water quality parameters to find the internal relationship with the optically inactive water quality parameters, and we will analyze the mechanism between the hyperspectral features and the retrieval objects.

4. Conclusion

Optically inactive water quality parameter estimation is a difficult task in water quality monitoring using remote sensing techniques, and the traditional semi-empirical and semi-analytical models cannot meet the accuracy requirements, especially in the complex bio-optical environment of inland water. In this study, we implemented deep learning based regression for the estimation of the optically inactive water parameters in an inland water body. The experiments showed the superiority of the deep learning based regression models in solving complex regression problems. Compared with the traditional machine learning models, the deep learning based model accuracy was greatly improved. The patch_DNNR model obtained a high prediction accuracy for all seven water quality parameters, especially for Zn, COD_{Mn}, TN, and TP, which all had Rp^2 values of greater than 0.8. After the accuracy evaluation, spatial distribution maps and water quality classification maps were generated using the hyperspectral imagery of the study area. Through the analysis of the laboratory test data and the on-site investigation of the research area, the spatial distribution maps were found to accurately reflect the actual situation, with the high-value regions distributed around the two large industrial parks and residential areas. In summary, the deep learning based regression models will be useful for water pollution monitoring, and could help government departments to

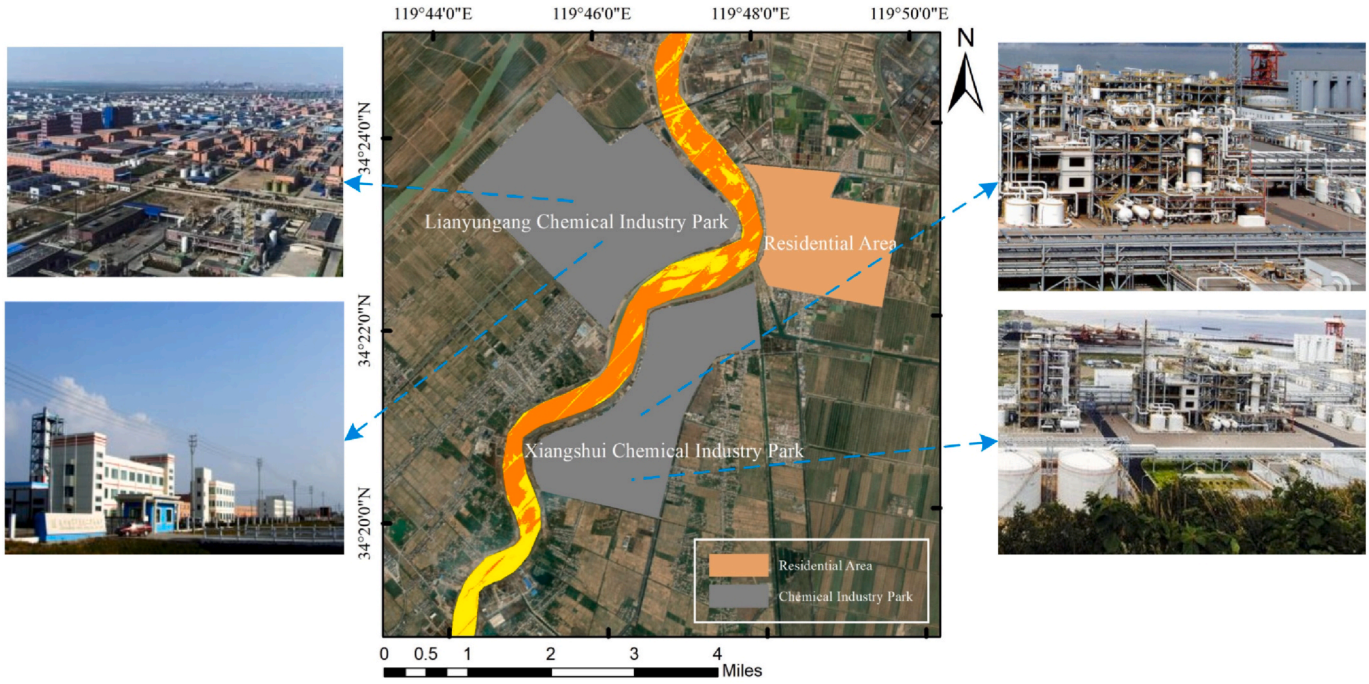

Fig. 7. Investigation and survey map of the pollution sources in the study area.

make pollution prevention and control decisions for inland water bodies.

Credit author statement

Chao Niu: Methodology, Software, Formal analysis, Writing- Original draft, Writing - Review & Editing. Kun Tan: Conceptualization, Supervision, Writing- Reviewing and Editing, Xiuping jia: Writing-Reviewing and Editing, Visualization. Xue Wang: Investigation, Writing - Review & Editing, Visualization.

Declaration of competing interest

The authors declare that they have no known competing financial interests or personal relationships that could have appeared to influence the work reported in this paper.

Acknowledgements

This research was supported in part by the National Natural Science Foundation of China (grant No. 41871337).

Appendix A. Supplementary data

Supplementary data to this article can be found online at https://doi.org/10.1016/j.envpol.2021.117534.

References

Allali, K., Bricaud, A., Claustre, H., 1997. Spatial variations in the chlorophyll-specific absorption coefficients of phytoplankton and photosynthetically active pigments in the equatorial Pacific. J. Geophys. Res.: Oceans 102, 12413–12423.
Brereton, R.G., Lloyd, G.R., 2010. Support vector machines for classification and regression. Analyst 135, 230–267.
Brezonik, P., Menken, K.D., Bauer, M., 2005. Landsat-based remote sensing of lake water quality characteristics, including chlorophyll and colored dissolved organic matter (CDOM). Lake Reservoir Manag. 21, 373–382.
Brooks, B.W., Lazorchak, J.M., Howard, M.D., Johnson, M.V.V., Morton, S.L., Perkins, D. A., Reavie, E.D., Scott, G.I., Smith, S.A., Steevens, J.A., 2016. Are harmful algal blooms becoming the greatest inland water quality threat to public health and aquatic ecosystems? Environ. Toxicol. Chem. 35, 6–13.
Carpenter, D., Carpenter, S., 1983. Modeling inland water quality using Landsat data. Rem. Sens. Environ. 13, 345–352.
Chang, C.-C., Lin, C.-J., 2011. LIBSVM: a library for support vector machines. ACM Transactions on Intelligent Systems and Technology 2, 1–27.
Chen, C., Liu, F., He, Q., Shi, H., 2010. The possibility on estimation of concentration of heavy metals in coastal waters from remote sensing data. In: 2010 IEEE International Geoscience and Remote Sensing Symposium. IEEE, pp. 4216–4219.
Chen, J., Zhu, W.-N., Tian, Y.Q., Yu, Q., 2017. Estimation of colored dissolved organic matter from Landsat-8 imagery for complex inland water: case study of Lake Huron. IEEE Trans. Geosci. Rem. Sens. 55, 2201–2212.
Dekker, A., Vos, R., Peters, S., 2001. Comparison of remote sensing data, model results and in situ data for total suspended matter (TSM) in the southern Frisian lakes. Sci. Total Environ. 268, 197–214.
Dekker, A.G., 1993. Detection of Optical Water Quality Parameters for Eutrophic Waters by High Resolution Remote Sensing. Ph.D. Thesis, Free University, Amsterdam, The Netherlards.
Dekker, A.G., Vos, R., Peters, S., 2002. Analytical algorithms for lake water TSM estimation for retrospective analyses of TM and SPOT sensor data. Int. J. Rem. Sens. 23, 15–35.
Di Noia, A., Hasekamp, O., van Harten, G., Rietjens, J., Smit, J., Snik, F., Henzing, J., de Boer, J., Keller, C., Volten, H., 2015. Use of neural networks in ground-based aerosol retrievals from multi-angle spectropolarimetric observations. Atmospheric Measurement Techniques 8, 281–299.
El Din, E.S., Zhang, Y., 2017. Estimation of both optical and nonoptical surface water quality parameters using Landsat 8 OLI imagery and statistical techniques. J. Appl. Remote Sens. 11, 046008.
El Din, E.S., Zhang, Y., Suliman, A., 2017. Mapping concentrations of surface water quality parameters using a novel remote sensing and artificial intelligence framework. Int. J. Rem. Sens. 38, 1023–1042.
Gholizadeh, M., Melesse, A., Reddi, L., 2016. A comprehensive review on water quality parameters estimation using remote sensing techniques. Sensors 16, 1298.
Gitelson, A.A., Dall'Olmo, G., Moses, W., Rundquist, D.C., Barrow, T., Fisher, T.R., Gurlin, D., Holz, J., 2008. A simple semi-analytical model for remote estimation of chlorophyll-a in turbid waters: Validation. Rem. Sens. Environ. 112, 3582–3593.
Gitelson, A.A., Merzlyak, M.N., 1997. Remote estimation of chlorophyll content in higher plant leaves. Int. J. Rem. Sens. 18, 2691–2697.
Gong, Z., Zhong, P., Yu, Y., Hu, W., Li, S., 2019. A CNN with multiscale convolution and diversified metric for hyperspectral image classification. IEEE Trans. Geosci. Rem. Sens. 57, 3599–3618.
Gordon, H.R., Brown, O.B., Evans, R.H., Brown, J.W., Smith, R.C., Baker, K.S., Clark, D. K., 1988. A semianalytic radiance model of ocean color. J. Geophys. Res.: Atmosphere 93, 10909–10924.
Han, L., 2005. Estimating chlorophyll-a concentration using first-derivative spectra in coastal water. Int. J. Rem. Sens. 26, 5235–5244.
Han, Z.-X., Lin, L., Fan, Y., Zou, C., 2018. Environmental risk assessment of the emerging EDCs contaminants in Guan river of Jiangsu in China. Acad. J. Sci. Res. 3.
Härmä, P., Vepsäläinen, J., Hannonen, T., Pyhälahti, T., Kämäri, J., Kallio, K., Eloheimo, K., Koponen, S., 2001. Detection of water quality using simulated satellite data and semi-empirical algorithms in Finland. Sci. Total Environ. 268, 107–121.

He, K., Zhang, X., Ren, S., Sun, J., 2016. Deep residual learning for image recognition. Proceedings of the IEEE conference on computer vision and pattern recognition 770–778.
Ioffe, S., Szegedy, C., 2015. Batch Normalization: Accelerating Deep Network Training by Reducing Internal Covariate Shift, International Conference on Machine Learning. PMLR, pp. 448–456.
Kallio, K., Kutser, T., Hannonen, T., Koponen, S., Pulliainen, J., Vepsäläinen, J., Pyhälahti, T., 2001. Retrieval of water quality from airborne imaging spectrometry of various lake types in different seasons. Sci. Total Environ. 268, 59–77.
Kar, D., Sur, P., Mandai, S., Saha, T., Kole, R., 2008. Assessment of heavy metal pollution in surface water. Int. J. Environ. Sci. Technol. 5, 119–124.
Keith, D.J., Schaeffer, B.A., Lunetta, R.S., Gould Jr., R.W., Rocha, K., Cobb, D.J., 2014. Remote sensing of selected water-quality indicators with the hyperspectral imager for the coastal ocean (HICO) sensor. Int. J. Rem. Sens. 35, 2927–2962.
Koponen, S., Pulliainen, J., Kallio, K., Hallikainen, M., 2002. Lake water quality classification with airborne hyperspectral spectrometer and simulated MERIS data. Rem. Sens. Environ. 79, 51–59.
Kutser, T., 2004. Quantitative detection of chlorophyll in cyanobacterial blooms by satellite remote sensing. Limnol. Oceanogr. 49, 2179–2189.
Kutser, T., Arst, H., Miller, T., Käärmann, L., Milius, A., 1995. Telespectrometrical estimation of water transparency, chlorophyll-a and total phosphorus concentration of Lake Peipsi. Int. J. Rem. Sens. 16, 3069–3085.
Kutser, T., Pierson, D.C., Kallio, K.Y., Reinart, A., Sobek, S., 2005. Mapping lake CDOM by satellite remote sensing. Rem. Sens. Environ. 94, 535–540.
LeCun, Y., Bengio, Y., 1995. Convolutional networks for images, speech, and time series. The handbook of brain theory and neural networks 3361, 1995.
Lei, S., Xu, J., Li, Y., Du, C., Liu, G., Zheng, Z., Xu, Y., Lyu, H., Mu, M., Miao, S., 2020. An approach for retrieval of horizontal and vertical distribution of total suspended matter concentration from GOCI data over Lake Hongze. Sci. Total Environ. 700, 134524.
Li, J., Chen, X., Tian, L., Huang, J., Feng, L., 2015. Improved capabilities of the Chinese high-resolution remote sensing satellite GF-1 for monitoring suspended particulate matter (SPM) in inland waters: radiometric and spatial considerations. ISPRS J. Photogrammetry Remote Sens. 106, 145–156.
Li, J., Yu, Q., Tian, Y.Q., Becker, B.L., 2017a. Remote sensing estimation of colored dissolved organic matter (CDOM) in optically shallow waters. ISPRS J. Photogrammetry Remote Sens. 128, 98–110.
Li, J., Zhao, R., Huang, J.-T., Gong, Y., 2014. Learning Small-Size DNN with Output-Distribution-Based Criteria, Fifteenth Annual Conference of the International Speech Communication Association, pp. 1910–1914.
Li, W., Wu, G., Zhang, F., Du, Q., 2016. Hyperspectral image classification using deep pixel-pair features. IEEE Trans. Geosci. Rem. Sens. 55, 844–853.
Li, Y., Xie, W., Li, H., 2017b. Hyperspectral image reconstruction by deep convolutional neural network for classification. Pattern Recogn. 63, 371–383.
Okujeni, A., van der Linden, S., Tits, L., Somers, B., Hostert, P., 2013. Support vector regression and synthetically mixed training data for quantifying urban land cover. Rem. Sens. Environ. 137, 184–197.
Olmanson, L.G., Brezonik, P.L., Bauer, M.E., 2013. Airborne hyperspectral remote sensing to assess spatial distribution of water quality characteristics in large rivers: the Mississippi River and its tributaries in Minnesota. Rem. Sens. Environ. 130, 254–265.
Palmer, S.C., Kutser, T., Hunter, P.D., 2015. Remote sensing of inland waters: challenges, progress and future directions. Rem. Sens. Environ. 157, 1–8.
Penuelas, J., Baret, F., Filella, I., 1995. Semi-empirical indices to assess carotenoids/chlorophyll a ratio from leaf spectral reflectance. Photosynthetica 31, 221–230.
Pyo, J., Duan, H., Baek, S., Kim, M.S., Jeon, T., Kwon, Y.S., Lee, H., Cho, K.H., 2019. A convolutional neural network regression for quantifying cyanobacteria using hyperspectral imagery. Rem. Sens. Environ. 233, 111350.
Pyo, J., Ligaray, M., Kwon, Y., Ahn, M.-H., Kim, K., Lee, H., Kang, T., Cho, S., Park, Y., Cho, K., 2018. High-spatial resolution monitoring of phycocyanin and chlorophyll-a using airborne hyperspectral imagery. Rem. Sens. 10, 1180.
Qian, Y., Fan, Y., Hu, W., Soong, F.K., 2014. On the Training Aspects of Deep Neural Network (DNN) for Parametric TTS Synthesis, 2014 IEEE International Conference on Acoustics, Speech and Signal Processing (ICASSP). IEEE, pp. 3829–3833.
Ritchie, J.C., Zimba, P.V., Everitt, J.H., 2003. Remote sensing techniques to assess water quality. Photogramm. Eng. Rem. Sens. 69, 695–704.
Schölkopf, B., Smola, A.J., Bach, F., 2002. Learning with Kernels: Support Vector Machines, Regularization, Optimization, and beyond. MIT press.
Schwarz, A., Huemmer, C., Maas, R., Kellermann, W., 2015. Spatial diffuseness features for DNN-based speech recognition in noisy and reverberant environments. In: 2015 IEEE International Conference on Acoustics, Speech and Signal Processing (ICASSP). IEEE, pp. 4380–4384.
Segal-Rozenhaimer, M., Li, A., Das, K., Chirayath, V., 2020. Cloud detection algorithm for multi-modal satellite imagery using convolutional neural-networks (CNN). Rem. Sens. Environ. 237, 111446.
Simis, S.G., Peters, S.W., Gons, H.J., 2005. Remote sensing of the cyanobacterial pigment phycocyanin in turbid inland water. Limnol. Oceanogr. 50, 237–245.
Singh, K.P., Basant, N., Gupta, S., 2011. Support vector machines in water quality management. Anal. Chim. Acta 703, 152–162.
Song, K., Li, L., Li, S., Tedesco, L., Hall, B., Li, L., 2012. Hyperspectral remote sensing of total phosphorus (TP) in three central Indiana water supply reservoirs. Water, Air, Soil Pollut. 223, 1481–1502.
Song, K., Li, L., Tedesco, L., Li, S., Duan, H., Liu, D., Hall, B., Du, J., Li, Z., Shi, K., 2013. Remote estimation of chlorophyll-a in turbid inland waters: three-band model versus GA-PLS model. Rem. Sens. Environ. 136, 342–357.
Srivastava, N., Hinton, G., Krizhevsky, A., Sutskever, I., Salakhutdinov, R., 2014. Dropout: a simple way to prevent neural networks from overfitting. J. Mach. Learn. Res. 15, 1929–1958.
Sun, D., Li, Y., Wang, Q., 2009. A unified model for remotely estimating chlorophyll a in Lake Taihu, China, based on SVM and in situ hyperspectral data. IEEE Trans. Geosci. Rem. Sens. 47, 2957–2965.
Tyler, A., Svab, E., Preston, T., Présing, M., Kovács, W., 2006. Remote sensing of the water quality of shallow lakes: a mixture modelling approach to quantifying phytoplankton in water characterized by high-suspended sediment. Int. J. Rem. Sens. 27, 1521–1537.
Vakili, T., Amanollahi, J., 2020. Determination of optically inactive water quality variables using Landsat 8 data: a case study in Geshlagh reservoir affected by agricultural land use. J. Clean. Prod. 247, 119134.
Wang, J.Z., Shi, T.Z., Yu, D.L., Teng, D.X., Ge, X.Y., Zhang, Z.P., Yang, X.D., Wang, H.X., Wu, G.F., 2020. Ensemble machine-learning-based framework for estimating total nitrogen concentration in water using drone-borne hyperspectral imagery of emergent plants: a case study in an arid oasis, NW China. Environ. Pollut. 266, 115412.
Wang, X., Tan, K., Du, Q., Chen, Y., Du, P., 2019. Caps-TripleGAN: GAN-assisted CapsNet for hyperspectral image classification. IEEE Trans. Geosci. Rem. Sens. 57, 7232–7245.
Wang, Z., Kawamura, K., Sakuno, Y., Fan, X., Gong, Z., Lim, J., 2017. Retrieval of chlorophyll-a and total suspended solids using iterative stepwise elimination partial least squares (ISE-PLS) regression based on field hyperspectral measurements in irrigation ponds in Higashihiroshima, Japan. Rem. Sens. 9, 264.
Wass, P., Marks, S., Finch, J., Leeks, G.J.L., Ingram, J., 1997. Monitoring and preliminary interpretation of in-river turbidity and remote sensed imagery for suspended sediment transport studies in the Humber catchment. Sci. Total Environ. 194, 263–283.
Williams, P., 1987. Variables Affecting Near-Infrared Reflectance Spectroscopic Analysis, Near-Infrared Technology in the Agricultural and Food Industries. American Association of Cereal Chemists, St. Paul, MN, pp. 143–167.
Xing, Q., Lou, M., Chen, C., Shi, P., 2013. Using in situ and satellite hyperspectral data to estimate the surface suspended sediments concentrations in the Pearl River estuary. IEEE Journal of Selected Topics in Applied Earth Observations and Remote Sensing 6, 731–738.
Xu, M., Liu, H., Beck, R., Lekki, J., Yang, B., Shu, S., Liu, Y., Benko, T., Anderson, R., Tokars, R., 2019. Regionally and locally adaptive models for retrieving chlorophyll-a concentration in inland waters from remotely sensed multispectral and hyperspectral imagery. IEEE Trans. Geosci. Rem. Sens. 57, 4758–4774.
Yang, J., Zhou, A., Han, L., Li, Y., Xie, Y., 2020. Monitoring urban black-odorous water by using hyperspectral data and machine learning. Environ. Pollut. 269, 116166.
Zhang, C., Wang, T., Atkinson, P.M., Pan, X., Li, H., 2015. A novel multi-parameter support vector machine for image classification. Int. J. Rem. Sens. 36, 1890–1906.
Zheng, J., Wang, Z., Lin, Z., 1982. A study of estuarine chemistry in the Zhujiang River II. Chemical forms of heavy metals in the suspended particulate. Oceanol. Limnol. Sinica 13, 523–530.